



UNIVERSITY OF LEEDS

This is a repository copy of *The interfacial reactivity of arsenic species with green rust sulfate (GRSO4)*.

White Rose Research Online URL for this paper:
<http://eprints.whiterose.ac.uk/147947/>

Version: Accepted Version

Article:

Perez, JPH, Freeman, HM orcid.org/0000-0001-8242-9561, Schuessler, JA et al. (1 more author) (2019) The interfacial reactivity of arsenic species with green rust sulfate (GRSO4). *Science of the Total Environment*, 648. pp. 1161-1170. ISSN 0048-9697

<https://doi.org/10.1016/j.scitotenv.2018.08.163>

© 2018, Elsevier B.V. This manuscript version is made available under the CC-BY-NC-ND 4.0 license <http://creativecommons.org/licenses/by-nc-nd/4.0/>.

Reuse

This article is distributed under the terms of the Creative Commons Attribution-NonCommercial-NoDerivs (CC BY-NC-ND) licence. This licence only allows you to download this work and share it with others as long as you credit the authors, but you can't change the article in any way or use it commercially. More information and the full terms of the licence here: <https://creativecommons.org/licenses/>

Takedown

If you consider content in White Rose Research Online to be in breach of UK law, please notify us by emailing eprints@whiterose.ac.uk including the URL of the record and the reason for the withdrawal request.



eprints@whiterose.ac.uk
<https://eprints.whiterose.ac.uk/>

1 **The interfacial reactivity of arsenic species with green rust sulfate (GR_{SO4})**

2
3 Jeffrey Paulo H. Perez^{a,b,*}, Helen M. Freeman^a, Jan A. Schuessler^{a,†}, Liane G. Benning^{a,b}

4
5 ^a GFZ German Research Center for Geosciences, Telegrafenberg, 14473 Potsdam, Germany

6 ^b Department of Earth Sciences, Free University of Berlin, 12249 Berlin, Germany

7
8 * Corresponding author: jpperez@gfz-potsdam.de

9 † Current address: Thermo Fisher Scientific GmbH, 28199 Bremen, Germany

10 11 **Abstract**

12 Arsenic (As) contamination in groundwater is a significant health and environmental concern
13 worldwide because of its wide distribution and toxicity. The fate and mobility of As is greatly
14 influenced by its interaction with redox-active mineral phases, among which green rust (GR), an Fe^{II}-
15 Fe^{III} layered double hydroxide mineral, plays a crucial role. However, the controlling parameters of
16 As uptake by GR are not yet fully understood. To fill this gap, we determined the interfacial reactions
17 between GR sulfate (GR_{SO4}) and aqueous inorganic As(III) and As(V) through batch adsorption
18 experiments, under environmentally-relevant groundwater conditions. Our data showed that, under
19 anoxic conditions, GR_{SO4} is a stable and effective mineral adsorbent for the removal of As(III) and
20 As(V). At an initial concentration of 10 mg L⁻¹, As(III) removal was higher at alkaline pH conditions
21 (~ 95% removal at pH 9) while As(V) was more efficiently removed at near-neutral conditions (>
22 99% at pH 7). The calculated maximum As adsorption capacities on GR_{SO4} were 160 mg g⁻¹ (pH 8-9)
23 for As(III) and 105 mg g⁻¹ (pH 7) for As(V). The presence of other common groundwater ions such as
24 Mg²⁺ and PO₄³⁻ reduces the efficiency of As removal, especially at high ionic strengths. Long-term
25 batch adsorption experiments (up to 90 days) revealed that As-interacted GR_{SO4} remained stable, with
26 no mineral transformation or release of adsorbed As species. Overall, our work shows that GR_{SO4} is
27 one of the most effective As adsorbents among iron (oxyhydr)oxide phases.

28
29 **Keywords:** arsenic; adsorption; green rust; groundwater treatment; iron (oxyhydr)oxide; layered
30 double hydroxide

32 1. Introduction

33 Elevated levels of dissolved arsenic (As) in ground- and drinking waters remain a significant
34 global environmental and public health concern because of the wide-spread occurrence and
35 distribution, as well as toxicity and mobility of As in the environment (Vaughan, 2006). In
36 groundwaters, As is commonly present as inorganic oxyanions arsenite ($\text{H}_3\text{As}^{\text{III}}\text{O}_3$) and arsenate
37 ($\text{H}_3\text{As}^{\text{V}}\text{O}_4$), with the former being the more toxic form (Hughes, 2002; Sharma and Sohn, 2009).
38 Based on their acid dissociation constants, As(III) forms the neutral species $\text{H}_3\text{As}^{\text{III}}\text{O}_3$ at moderately
39 reducing conditions ($\text{pK}_{\text{a}1,2,3} = 9.23, 12.13, 13.40$) while As(V) is present as $\text{H}_2\text{As}^{\text{V}}\text{O}_4^-$ and $\text{HAs}^{\text{V}}\text{O}_4^{2-}$
40 ($\text{pK}_{\text{a}1,2,3} = 2.20, 6.97, 11.53$) in oxidized environments (Ferguson and Gavis, 1972; Inskeep et al.,
41 2002). However, it is important to note that the relatively slow redox transformation kinetics allows
42 both As(III) and As(V) to persist under both anoxic and oxic conditions (Masscheleyn et al., 1991).

43 Green rust (GR) minerals are redox-active phases, which belong to the family of $\text{Fe}^{\text{II}}\text{-Fe}^{\text{III}}$
44 layered-double hydroxides (LDHs). Their ability to treat or remove toxic metals from groundwater
45 has been investigated (Usman et al., 2018), yet the fundamental adsorption properties or uptake
46 capacities of metals on GR phases have still not been quantified. The high potential of GR as a
47 material for groundwater remediation stems from its structural and redox properties. GR is composed
48 of positively charged brucite-like layers of octahedrally coordinated $\text{Fe}^{\text{II}}\text{-Fe}^{\text{III}}$ hydroxides that alternate
49 with negatively charged interlayers of anions and water molecules, as well as monovalent cations
50 (Christiansen et al., 2009). These brucite-like layers and interlayer regions are held together by
51 hydrogen bonding and electrostatic forces. GR is typically represented by the general formula, $[\text{Fe}^{\text{II}}_{(1-x)}\text{Fe}^{\text{III}}_x(\text{OH})_2]^{x+}[(x/n) \text{A}^{n-} \cdot m\text{H}_2\text{O}]^x$, where A^{n-} is the intercalated anion such as Cl^- , CO_3^{2-} and SO_4^{2-} , and
52 x is the molar fraction of Fe^{III} , $[\text{Fe}^{\text{III}}]/[\text{Fe}_{\text{total}}]$ (Géhin et al., 2002). These properties allow GR to
53 remove toxic metal contaminants by adsorption (Jönsson and Sherman, 2008; Mitsunobu et al., 2009),
54 reduction (Christiansen et al., 2011; O'Loughlin et al., 2003; Skovbjerg et al., 2006), interlayer
55 intercalation (Refait et al., 2000), and substitution of structural Fe in the octahedral sheets (Ahmed et
56 al., 2008; Refait et al., 1990).

58 Considering the worldwide health implications of As-contaminated ground- and drinking
59 waters (World Health Organization, 2017), it is paramount that we understand the removal efficiency

60 of As through interactions with various mineral substrates. There is an imminent challenge regarding
61 the development, testing and validating the usefulness of adequate mineral phases that have high
62 metal-specific uptake capacities, strong binding affinities and excellent stabilities. Adsorption-based
63 technologies are promising groundwater clean-up strategies because of their facile implementation,
64 relative cost-effectiveness and high removal efficiency (Leus et al., 2017). However, to optimize the
65 efficiency of subsurface remediation strategies, the interactions between inorganic As species and the
66 surfaces of redox-active minerals such as GR must be quantified in detail.

67 Su and Wilkin (2005) examined the interaction of As(III) and As(V) with synthetic green rust
68 carbonate (GR_{CO_3}) and monitored the changes in the aqueous phase. Their results showed that As(V)
69 removal rates using GR_{CO_3} were higher compared to As(III) due to the higher affinity of iron
70 (oxyhydr)oxides for As(V) than the more toxic As(III). The mechanism of adsorption of As species
71 onto GR mineral phases (e.g., GR_{Cl} , GR_{CO_3} , GR_{SO_4}) has also been investigated previously using X-ray
72 absorption spectroscopy (XAS) (Jönsson and Sherman, 2008; Randall et al., 2001; Wang et al., 2010).
73 In these studies, As(III) and As(V) were found to both form bidentate binuclear (^2C) and monodentate
74 mononuclear (^1V) inner-sphere complexes on the FeO_6 octahedra at the edges of the GR crystal.
75 However, the fundamental adsorption parameters (e.g., effects of pH, adsorbent loading, ionic
76 strength, potentially competing ions), as well as the maximum uptake capacity and critical adsorption
77 kinetics, necessary for understanding interactions between GR and As in groundwaters have never
78 been evaluated in detail.

79 Herein, we aim to close this gap through an in-depth investigation on the interfacial
80 interactions between freshly-precipitated green rust sulfate (GR_{SO_4}) and aqueous inorganic As species.
81 We evaluated the performance of GR_{SO_4} as an effective adsorbent for the removal of arsenite [As(III)]
82 and arsenate [As(V)] by examining adsorption reactions as a function of pH, adsorbent loading, ionic
83 strength, varying initial As concentrations, time and the presence of potentially interfering ions in
84 groundwater. Our results reveal that GR_{SO_4} is a highly effective adsorbent for the removal of As
85 species from groundwater.

86

87

88 2. Materials and methods

89 2.1 Mineral synthesis and characterization

90 GR with interlayer sulfate (GR_{SO_4}) was synthesized in an anaerobic chamber (95% N_2 , 5% H_2 ,
91 Coy Laboratory Products, Inc.) at room temperature using the co-precipitation method (Géhin et al.,
92 2002). In brief, separate Fe(II) (0.3 M) and Fe(III) (0.1 M) solutions were prepared from reagent
93 grade $(\text{NH}_4)_2\text{Fe}(\text{SO}_4)_2 \cdot 6\text{H}_2\text{O}$ and $\text{Fe}_2(\text{SO}_4)_3$ salts (VWR) and deoxygenated Milli-Q water ($\sim 18.2 \text{ M}\Omega$
94 cm^{-1}). GR synthesis was initiated by mixing the Fe(III) and Fe(II) solutions (pH ~ 2) under constant
95 stirring at 350 rpm. Subsequently, a 0.3 M NaOH solution was slowly titrated into the mixed $\text{Fe}^{\text{II}}\text{-Fe}^{\text{III}}$
96 solution until the pH reached 8. Base addition resulted in the precipitation of a dark blue-green
97 suspension, which was stirred and aged further for one hour. The suspension was then washed with
98 O_2 -free Milli-Q water to remove excess solutes. The yield of the washed GR_{SO_4} slurry was determined
99 based on the difference between the total Fe concentration of an aliquot of the suspension dissolved in
100 0.3 M HNO_3 and the dissolved Fe concentration in the supernatant after filtration through a 0.2- μm
101 syringe filter. The Fe ion concentration was analyzed by inductively coupled plasma optical emission
102 spectrometry (ICP-OES). Each batch of GR_{SO_4} slurry ($\sim 8.2 \text{ g L}^{-1}$) was prepared fresh and kept in the
103 anaerobic chamber adsorption experiments for a maximum of 24 h.

104 The solid GR_{SO_4} samples were analyzed by X-ray powder diffraction (XRD), nitrogen
105 sorption, transmission electron microscopy (TEM), selected area electron diffraction (SAED), energy
106 dispersive X-ray spectroscopy (EDX), electron energy-loss spectroscopy (EELS), high angle annular
107 dark field scanning transmission electron microscopy (HAADF-STEM), X-ray photoelectron
108 spectroscopy (XPS) and Mössbauer spectroscopy to determine their structure, particle sizes,
109 morphologies, surface properties, as well as redox and full chemical composition. Detailed
110 information on all phase characterizations can be found in the Supporting Information (Text S1).

111

112 2.2 Adsorption experiments

113 All batch adsorption experiments were carried out in triplicate at room temperature inside the
114 anaerobic chamber using headspace crimp vials with the washed GR_{SO_4} suspensions ($\text{S/L} = 4 \text{ g L}^{-1}$)
115 reacted with 10 mg L^{-1} aqueous As(III) or As(V) solutions. The mixed samples were shaken at 250

116 rpm for 24 h followed by the separation of solids and supernatants by filtration through 0.22- μ m
117 syringe filters. The obtained liquid phases were acidified (pH \sim 2 with Merck Suprapur[®] grade HNO₃)
118 and stored at 4°C until analysis. The elemental composition of the liquid phases was determined
119 following the method described in Schuessler et al. (2016) using an axial ICP-OES Varian 720ES.
120 Full details of all tested parameters [e.g., varying pH (7 to 9), adsorbent loading (solid to solution
121 ratio, S/L 2 to 6 g L⁻¹), ionic strength (IS* 0.5 to 0.005 M), competing ions (Ca²⁺, Mg²⁺, PO₄³⁻) and
122 time (5 min to 90 days)] for the batch adsorption experiments and analytical methods can be found in
123 the Supporting Information (Text S1, Table S1).

124

125 2.3 Adsorption kinetics and isotherms

126 Kinetic rates of As adsorption were determined at pH 8 using an initial As concentration of 10
127 mg L⁻¹ and an adsorbent loading of 4 g L⁻¹. The mixtures were shaken for 5 min, 10 min, 15 min, 30
128 min, 1 h, 2 h, 4 h, 8 h, 16 h and 24 h after which the solids were separated from the supernatant and
129 analysed as described above. Adsorption isotherms were obtained at room temperature and at pH 7
130 and 8-9 using an adsorbent loading of 4 g L⁻¹, initial As concentrations up to 1,000 mg L⁻¹ and contact
131 time of 24 h. The obtained equilibrium adsorption data were fitted to the Langmuir and Freundlich
132 isotherm models (Limousin et al., 2007).

133

134 3. Results and discussion

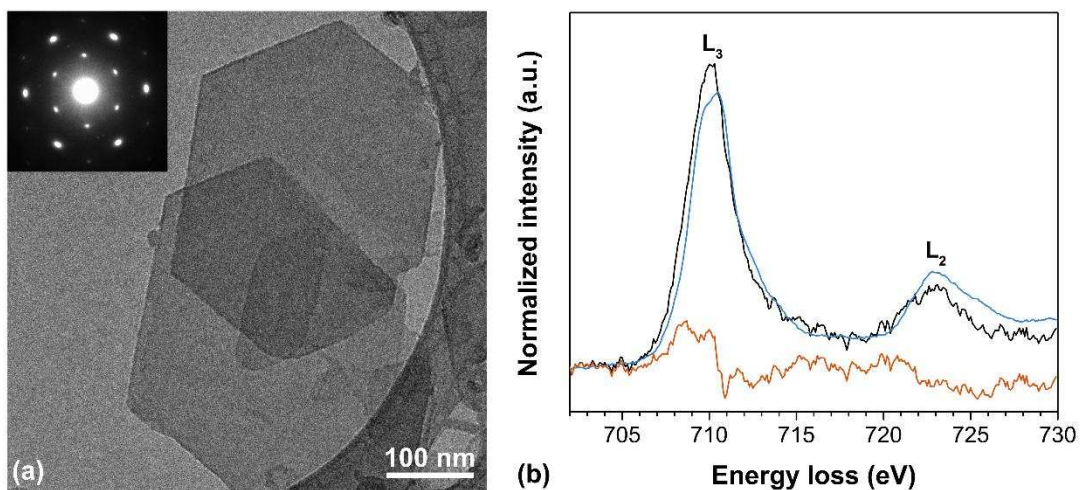
135 3.1 Synthesis and characterization of GR_{SO4}

136 The morphology, size and chemical composition of the synthesized GR_{SO4} particles were
137 characterized by TEM imaging and analytical spectroscopy. The micrographs (Fig. 1a) of the
138 synthesized material revealed a well-defined hexagonal plate-like morphology typical of GR_{SO4}
139 (Géhin et al., 2002). The diameter of particles varied between 50 and 500 nm while the estimated
140 thickness of the particles calculated by the log-ratio (relative) method (Malis et al., 1988) from the
141 low loss EEL spectra was around 16 to 20 nm. The SAED pattern (Fig. 1a inset) shows the distinctive
142 hexagonal c-axis spot pattern of a single crystal GR_{SO4} (Ahmed et al., 2010). The elemental
143 composition (Table S2), which was calculated from the EDX spectra, is comparable to the theoretical

144 values based on the chemical formula, $\text{Fe}^{\text{II}}_4\text{Fe}^{\text{III}}_2(\text{OH})_{12}\text{SO}_4 \cdot 8\text{H}_2\text{O}$ (Simon et al., 2003). The
145 mineralogy of the freshly-precipitated material was confirmed through XRD patterns (Fig. S1) to be
146 pure GR_{SO_4} as evidenced through the typical sharp and symmetric basal (001) reflections
147 corresponding to the interlayer distances between the $\text{Fe}^{\text{II}}\text{-Fe}^{\text{III}}$ octahedral hydroxide sheets (Simon et
148 al., 2003). No other iron (oxyhydr)oxide phases were identified in the freshly-precipitated GR_{SO_4}
149 samples.

150 The oxidation state of Fe can be determined by the EELS Fe L_3 -edge position and shape,
151 where octahedrally coordinated Fe(III) has a peak energy ~ 1.8 eV higher than octahedrally
152 coordinated Fe(II) (Brown et al., 2017). Separate peaks attributed to Fe^{2+} (709 eV) and Fe^{3+} (710.8
153 eV) within the primary L_3 peak are resolvable when EEL spectra are acquired at higher resolution
154 EELS (< 0.3 eV). Using the EELS resolution of the microscope used for this work (0.8 eV), the
155 Fe(II)/Fe(III) ratio was estimated by comparing our experimental spectra to reference spectra
156 collected under the same conditions. Theoretical spectra were calculated by stoichiometrically
157 combining the intensity-normalized spectra of the Fe standards for hedenbergite (octahedrally
158 coordinated Fe^{2+}) and hematite (octahedrally coordinated Fe^{3+}). This resulted in a theoretical spectrum
159 for GR_{SO_4} (where $\text{Fe(II)/Fe(III)} = 2$) which allowed for the direct comparison between the Fe L_3 peak
160 shape and position in our sample and the theoretical spectrum (blue line in Fig. 1b; Fig. S2a). This
161 revealed that the shape of the Fe L_3 -edge for the GR_{SO_4} sample matched the linear reference fit for a
162 Fe(II)/Fe(III) ratio of 2, with minor differences. This is evidenced by the changes in shape and
163 position of the L_3 peak in the theoretical spectrum as the GR composition becomes more Fe(III)-rich.
164 This is also clearly shown in Fig. S2, where the theoretical spectra for Fe(II)/Fe(III) ratios from 1 to
165 0.2, and the residual of each fit are shown. These results suggest that our sample had a Fe(II)/Fe(III)
166 ratio corresponding to 2.

167

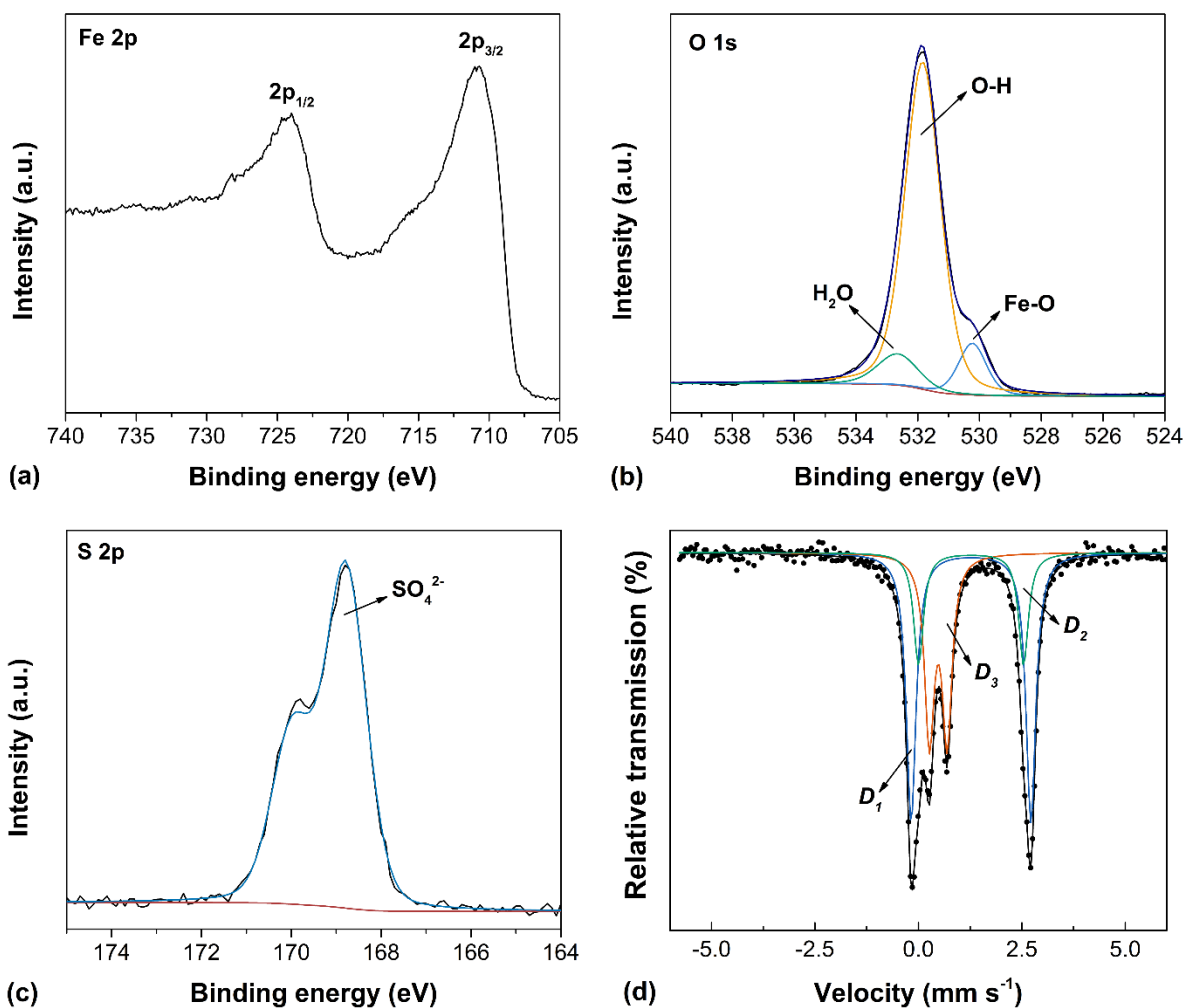


168
 169 **Fig. 1.** (a) TEM image of GR_{SO4} with SAED pattern of a single particle in inset. (b) Fe L_{2,3}-edge EEL
 170 spectrum of GR_{SO4} sample (black), linear reference fit (blue) and residual spectrum (orange).

171
 172 The surface chemistry of the synthesized GR_{SO4} was analyzed by XPS and the wide scan
 173 spectrum (Fig. S3) revealed photoelectron peaks of Fe 2p, O 1s and S 2p at binding energies of 710.7,
 174 531.9 and 168.8 eV, respectively. The Fe 2p_{1/2} and 2p_{2/3} photoelectron peaks (Fig. 2a) were observed
 175 at 724.0 and 710.7 eV, respectively. The value of the Fe 2p_{2/3} peak maxima was shifted to slightly
 176 higher binding energy compared to a GR with interlayer carbonate (GR_{CO3}, 709.4 eV), which also has
 177 an Fe(II)/Fe(III) ratio of 2.0 (Mullet et al., 2008). This indicates a slightly higher Fe(III) content in our
 178 synthesized GR_{SO4}. However, the presence of a characteristic Fe(II) satellite peak at 726.7 eV and a
 179 Fe(III) satellite peak at 731.0 eV confirmed the presence of both Fe(II) and Fe(III) in our sample at
 180 the desired ratio of 2. The peak shape and positions of the Fe 2p_{1/2} and 2p_{2/3} photoelectron peaks were
 181 also similar to previously reported XPS spectra for GR_{SO4} (Nedel et al., 2010). Furthermore, the
 182 relative contributions of the deconvoluted O 1s peaks at 530.2, 531.8 and 532.6 eV (Fig. 2b) that were
 183 assigned to Fe-O, O-H and adsorbed water (Table S3), respectively, were in agreement with values
 184 obtained by Mullet et al. (2008). The S 2p doublet (Fig. 2c) at 168.8 eV confirmed the presence of
 185 SO₄²⁻ in the interlayer region.

186 The iron chemistry of the synthesized GR_{SO4} was characterized by Mössbauer spectroscopy
 187 which revealed two apparent doublets (Fig. S3), but with a certain line broadening of the outer
 188 doublet and a slight asymmetry of its line shape. An improved fit shown in Fig. 2d was obtained by

189 using three doublets D_1 , D_2 and D_3 (hyperfine parameters, see Table S4). In this fit, doublets D_1 and
190 D_2 correspond to high spin Fe(II) cations in the brucite-like octahedral sheets while doublet D_3
191 corresponds to high spin Fe(III) cations (Géhin et al., 2002). The relative areas of the doublets in the
192 Mössbauer spectrum allowed us to calculate an Fe(II)/Fe(III) ratio in the GR_{SO_4} sample of 2.09, which
193 is in agreement with the ratio of 2 from our EELS data (Fig. 1b, Fig S2), as well as literature data
194 (Géhin et al., 2002; Simon et al., 2003). However, it should be noted that the Mössbauer spectra for
195 GR_{SO_4} reported in literature are usually fitted with one Fe(II) doublet (Fig. S3, Table S5) instead of
196 two doublets (Fig. 2d). It is worth noting nevertheless, that in our GR_{SO_4} , the two doublets D_1 and D_2
197 revealed the same isomer shift, but these differed somewhat in their quadrupole splittings (ΔE_Q),
198 thereby suggesting the presence of two inequivalent Fe(II) sites. The component with the largest ΔE_Q
199 was attributed to Fe(II) ions far away from the anions (Géhin and Ruby, 2004), whereas the presence
200 of a component with smaller ΔE_Q suggested the presence of Fe(II) sites containing anions in their
201 environment. Such components have been previously observed in Mössbauer spectra of GR samples
202 with other interlayer anions like carbonate or chloride but not for sulfate (Géhin and Ruby, 2004).
203



204 (c) Binding energy (eV)

205 **Fig. 2.** (a-c) High resolution XPS spectra of GR_{SO₄}: (a) Fe 2p, (b) O 1s and (c) S 2p spectra. (d) ⁵⁷Fe

206 Mössbauer spectrum of GR_{SO₄} recorded at 20 K and fitted with three doublets.

207

208 3.2 Influence of environmental parameters on As removal

209 The effect of pH, adsorbent loading (solid to liquid ratio, S/L), ionic strength (IS*) and the

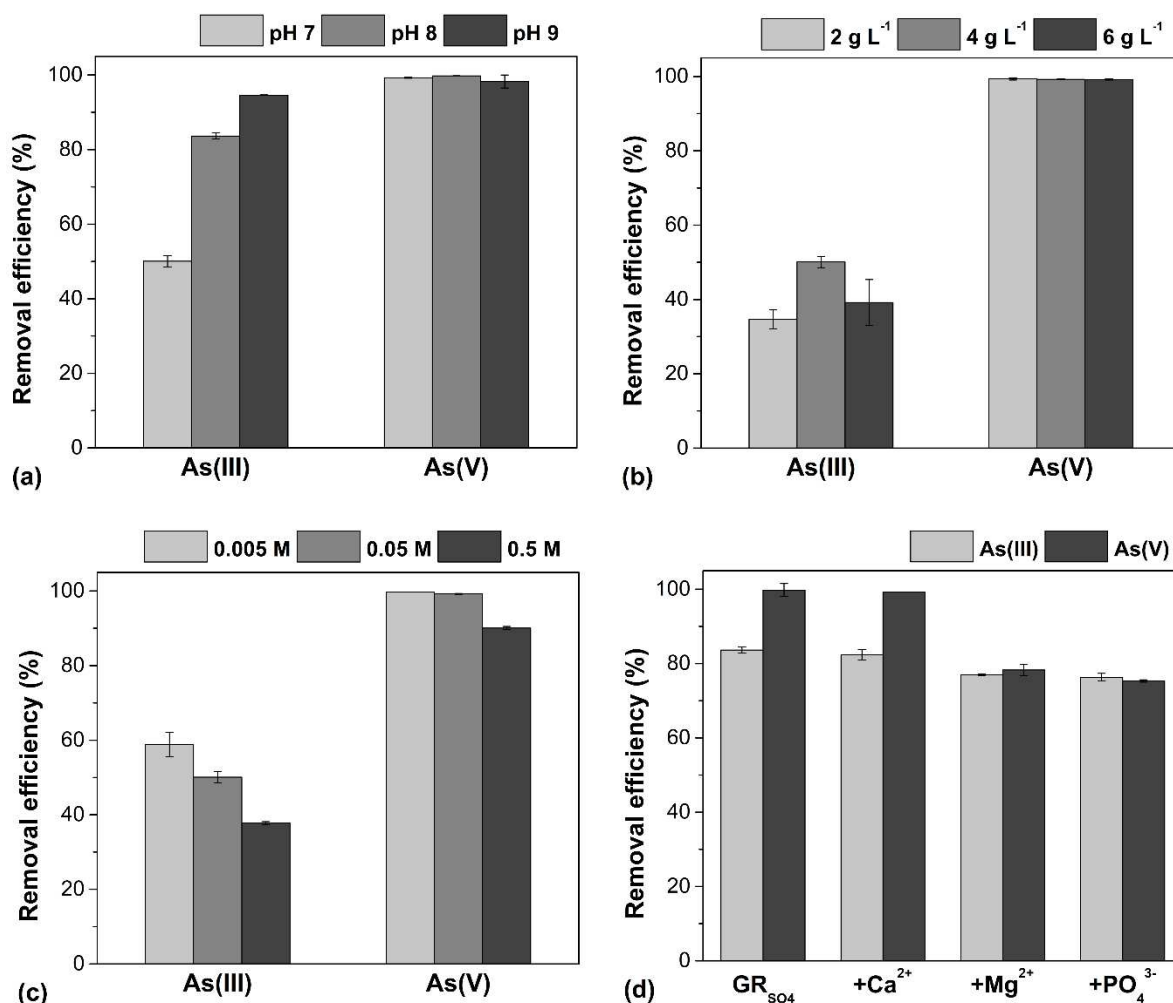
210 presence of other potentially interfering aqueous groundwater ions were investigated to determine

211 their influence on the adsorption of As species on GR_{SO₄}. The removal efficiencies of GR_{SO₄} for

212 As(III) and As(V) at an initial concentration of 10 mg L⁻¹ and under the above mentioned varying

213 conditions are shown in Fig. 3.

214



215

216 **Fig. 3.** Removal of 10 mg L⁻¹ As(III) and As(V) upon interaction with GR_{SO4} after 24 h as a function
 217 of: (a) pH (S/L = 4 g L⁻¹, IS* = 0.05 M), (b) adsorbent loading, S/L (pH 7, IS* = 0.05 M), (c) ionic
 218 strength, IS* (pH 7, S/L = 4 g L⁻¹) and (d) presence of competing groundwater ions (at pH 8 and IS* =
 219 0.05 M): pure GR_{SO4} (no competing ion), Ca²⁺ (100 mg L⁻¹), Mg²⁺ (50 mg L⁻¹) or PO₄³⁻ (10 mg L⁻¹).
 220 Error bars represent standard deviations of triplicate experiments (< 5% relative). Note: IS* here is
 221 defined as the ionic strength based on a 10x and 100x dilution from the initial 0.5 M IS of the GR_{SO4}
 222 suspension (further details, see in Supporting Information Text S1).

223

224 At all pH values tested, the As(V) removal efficiencies (Fig. 3a) were higher compared to
 225 As(III). This is likely because of the higher adsorption affinity of the pentavalent species on iron
 226 (oxyhydro)oxide surfaces. No significant differences in As(V) removal efficiencies between pH 7, 8
 227 and 9 were observed (i.e. within analytical uncertainties < 2%). Although there were no significant

228 differences in removal efficiencies, GR_{SO4} can effectively remove As(V) at a relatively wide range of
229 pH conditions that can be found in contaminated groundwaters (Nickson et al., 2000; Smedley and
230 Kinniburgh, 2002; Zahid et al., 2008). In contrary, the removal efficiency of As(III) by GR_{SO4} was
231 significantly affected by pH, which is the opposite of what was expected. With pH, As(III) removal
232 efficiency ($50.1 \pm 1.5\%$ at pH 7) increased by more than 30% at pH 8 ($83.7 \pm 0.9\%$) and another 10%
233 increase was measured at pH 9 ($94.6 \pm 0.1\%$). Such surface polymerization of As(III) complexes has
234 been previously suggested for GR_{Cl} and GR_{CO3} by XAS analysis (Ona-Nguema et al., 2009; Wang et
235 al., 2010). Usually, the influence of pH on As adsorption by iron (oxy)hydroxides is controlled by two
236 factors: (1) the speciation of the As in solution and (2) the point of zero charge (PZC) of the
237 adsorbent. Over the pH range tested here, As(III) will mostly exist as $H_3AsO_3^0$ and $H_2AsO_3^-$ species
238 while As(V) is present as $H_2AsO_4^-$ and $HAsO_4^{2-}$ species (Jain et al., 1999). For GR_{SO4} with a PZC of
239 8.3 (Guilbaud et al., 2013), the net surface charges will be negative at $pH > 8.3$ and positive at $pH <$
240 8.3 . As a result of electrostatic repulsion caused by similar negative charges, one would expect the
241 removal of both As(III) and As(V) species to decrease as the pH is increased from 8 to 9, which was
242 not observed in our study. Particularly, for As(III), the biggest increase in removal was observed
243 between pH 7 and 8 with a lesser change between 8 and 9 (Fig. 3a.). Similar trends have been
244 observed for As interacted with GR_{CO3} (Jönsson and Sherman, 2008) and ferrihydrite (Jain et al.,
245 1999; Raven et al., 1998). An increased As(III) adsorption at higher pH can be attributed to the
246 possible formation of multi-nuclear complexes on the surfaces of GR_{SO4}.

247 With increased adsorbent loading from 2 to 4 g L⁻¹, the removal efficiency of As(III) also
248 increased by ~15% from 34.6 ± 2.7 to $50.1 \pm 1.5\%$ (Fig. 3b). This increase was caused by the larger
249 number of active surface sites available for As(III) complexes (Asere et al., 2017). However, with
250 further increase in loading to 6 g L⁻¹, the efficiency decreased to $39.2 \pm 6.2\%$. In the case of As(V), no
251 significant differences (< 0.3% relative) in removal efficiencies were observed among the adsorbent
252 loadings tested (Fig. 3b).

253 The removal efficiencies for both As species decreased with increasing ionic strength, IS*
254 (Fig. 3c). For As(V), this decrease was only about 10% (from > 99.8 to $90.1 \pm 0.4\%$) as ionic strength
255 increased from 0.005 to 0.5 M. On the other hand, this inhibitory effect was more pronounced for

256 As(III) where the removal efficiency decreased $58.9 \pm 3.2\%$ at an ionic strength of 0.005 M to $37.8 \pm$
257 0.4% at an ionic strength of 0.5 M, although the overall removal was lower compared to As(V). The
258 decrease in As removal at higher IS* can be caused by the decrease in available surface sites of
259 GR_{SO4}. This results from potential aggregation of GR_{SO4} particles due to disturbances in the
260 electrostatic double layer (Shipley et al., 2009). Although the presence of ionic species in the
261 supernatant can also decrease the removal efficiency, the dissolved solutes in our experiments (e.g.,
262 Fe²⁺, NH₄⁺, Na⁺, Cl⁻ and SO₄²⁻ ions) have been shown to have little or no effect on As adsorption
263 (Asere et al., 2017; Guo and Chen, 2005; Gupta et al., 2009).

264 Common aqueous groundwater ions can compete for the available active surface sites on
265 GR_{SO4} (Folens et al., 2016; Leus et al., 2018). We tested the effect of relevant dissolved potentially
266 interfering ions in the water matrix through competitive adsorption experiments with Ca²⁺ (100 mg L⁻¹)
267 ¹), Mg²⁺ (50 mg L⁻¹) or PO₄³⁻ (10 mg L⁻¹) and As (10 mg L⁻¹) to the GR_{SO4} suspension at pH 8. The
268 concentrations of the competing ions were chosen based on the average aqueous ion concentrations in
269 As-contaminated groundwaters in Bangladesh and West Bengal, India (Nickson et al., 2000; Zahid et
270 al., 2008) and mining-contaminated groundwater sites (Smedley and Kinniburgh, 2002; Williams et
271 al., 1996). The comparison (Fig. 3d) revealed no significant change in the removal of As(III) and
272 As(V) resulting from the presence of Ca²⁺ ions. On the other hand, the presence of Mg²⁺ ions
273 decreased the removal efficiency by $6.7 \pm 1.0\%$ for As(III) and $21.5 \pm 2.1\%$ As(V) compared to the
274 Mg²⁺ free system. However, analysis of the liquid phases by ICP-OES revealed that Mg²⁺ was not
275 adsorbed on GR_{SO4}, but remained solvated in the supernatant. This decrease in As removal can be
276 caused by the high ionic potential of Mg²⁺, allowing it be solvated by water molecules (Lightstone et
277 al., 2001) and resulting in the formation outer-sphere hydrated Mg²⁺ complexes. Such aqueous
278 complexes could potentially reduce the accessibility of active surface sites of GR_{SO4} for As
279 adsorption. The presence of PO₄³⁻ ions also resulted in the inhibition of As adsorption, where the
280 removal efficiency for As(III) and As(V) decreased by 7.3 ± 1.3 and $24.5 \pm 1.8\%$, respectively.
281 Phosphate, with a tetrahedral molecular geometry analogous to the structure of AsO₄³⁻, can also form
282 complexes in the same lateral (010) and (100) GR surfaces sites where As complexes bind (Bocher et
283 al., 2004). This can result in a competition between PO₄³⁻ and As species on the available GR_{SO4}

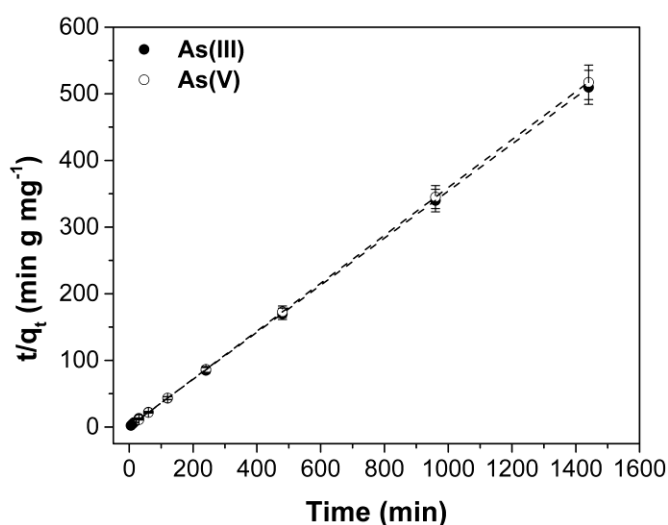
284 binding sites, thereby explaining the reduced As removal efficiency. Remarkably, the phosphate
285 removal efficiency was > 90% for both the As(III) and As(V) competitive adsorption experiments.
286 This likely results from the higher affinity of iron (oxyhydr)oxides for phosphate compared to As, as
287 indicated by its higher sorption equilibrium constant (Roberts et al., 2004), and the slow exchange of
288 initially adsorbed phosphate on the GR_{SO4} surface sites with the competing As species (Hongshao and
289 Stanforth, 2001).

290

291 3.3 Adsorption kinetics

292 The rate of As removal over 24 h was determined at pH 8 by measuring the adsorption
293 kinetics in batch experiments at initial As concentration of 10 mg L⁻¹ As(III) or As(V), S/L of 4 g L⁻¹
294 and an ionic strength of 0.05 M. After fitting the kinetic data with various adsorption models, the best
295 fit ($R^2 > 0.9999$) resulted from the pseudo-2nd order kinetic model (Ho, 2006). The linearized plots for
296 the pseudo-2nd order kinetic model are shown in Fig. 4. The calculated adsorption rate constants (k_2 ;
297 Table S6) revealed that the uptake of both As species was very fast. Full adsorption (> 99% removal)
298 of As(V) was achieved within 30 min of contact with GR_{SO4}, while As(III) reached equilibrium after 4
299 h. The more rapid removal of As(V) was caused by the stronger binding affinity of pentavalent over
300 the trivalent As species to iron (oxyhydr)oxides (Roberts et al., 2004). These fast adsorption uptake
301 rates show that GR_{SO4} can efficiently remove As(III) and As(V) within a short time.

302



303

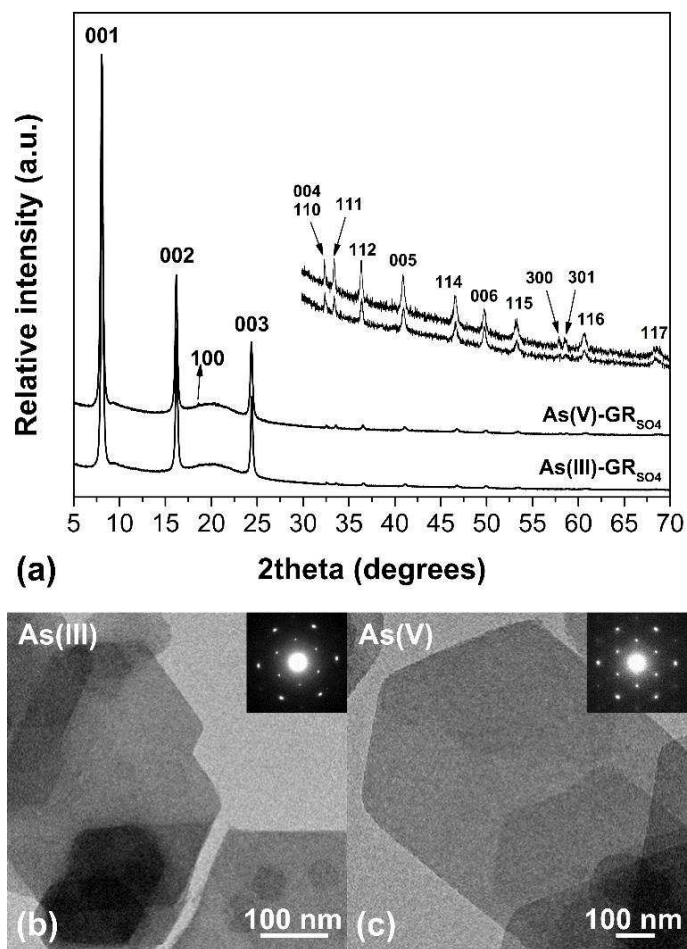
304 **Fig. 4.** Pseudo-2nd order kinetic data and model fits for the adsorption of As species on GR_{SO4}. Initial
305 concentration is 10 mg L⁻¹ at pH 8, S/L ratio of 4 g L⁻¹ and IS* of 0.05 M. Error bars represent
306 analytical uncertainty (< 5% relative) based on replicate measurements of QC solutions analyzed
307 together with the samples (Table S1).

308

309 3.4 Long-term batch adsorption experiments

310 At an initial As concentration of 10 mg L⁻¹, GR_{SO4} remained stable during the course of the
311 90-day monitoring of batch adsorption experiments. No other iron (oxyhydr)oxide mineral phases
312 were identified in XRD patterns of these long-term equilibrated and As-interacted samples (Fig. 5a).
313 The TEM images and SAED patterns (Fig. 5b) also showed that the GR_{SO4} particles in the 90-day
314 long interacted samples maintained their well-defined thin hexagonal plate-like morphology and
315 crystal structure. These observations were also confirmed by the fact that the long-term monitoring of
316 aqueous As in the supernatant (Fig. S6) revealed that the initial adsorbed As was not released back
317 into the aqueous phase. Previous studies have shown that adsorbed As can slow down or inhibit the
318 transformation of GR minerals to other iron (oxyhydr)oxides such as magnetite (Su and Wilkin, 2005;
319 Wang et al., 2014), which explains the stability of the As-interacted GR_{SO4} even after 90 days in our
320 study. In addition, our results are also consistent with long-term batch experiments of Su and Wilkin
321 (2005), who showed that As-interacted GR_{CO3} remained stable for up to 60 days.

322



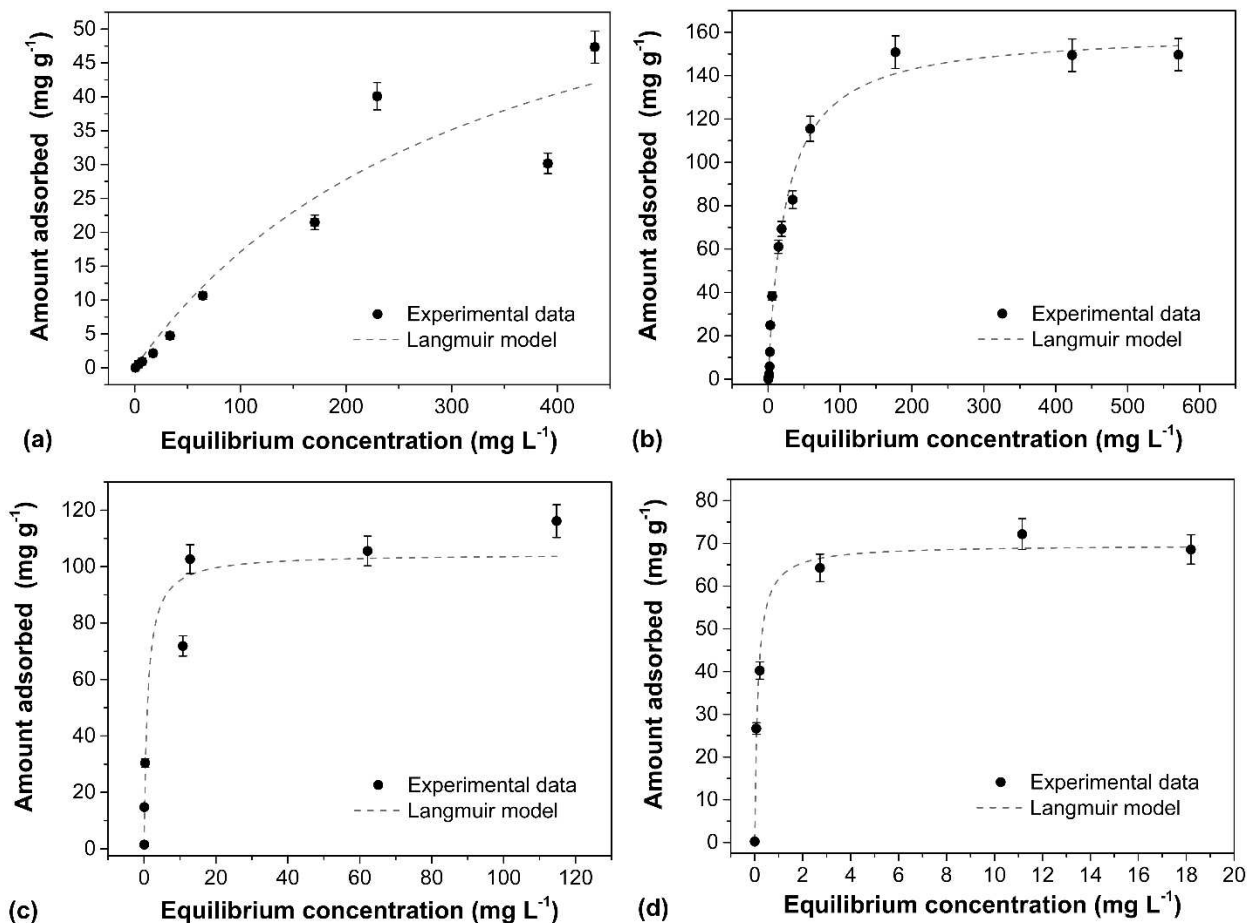
323
 324 **Fig. 5.** (a) XRD patterns and (b-c) TEM images (inset: SAED pattern) GR_{SO_4} interacted with 10 mg L^{-1}
 325 $As(III)$ and $As(V)$ after 90 days. XRD peaks of GR_{SO_4} were assigned based on published diffraction
 326 data (Simon et al., 2003). The broad amorphous hump at $\sim 20^\circ$ 2θ comes from the XRD sample
 327 holder.

328

329 3.5 Adsorption isotherms and mechanism

330 The As adsorption isotherms at all tested pH values are shown in Fig. 6. Equilibrium
 331 adsorption data were fitted to Langmuir and Freundlich isotherm models and the calculated fitting
 332 parameters for both models are shown in Table S7. Based on the fitting, the adsorption of As species
 333 on GR_{SO_4} is best described using the Langmuir model, indicating a homogenous monolayer binding of
 334 As surface complexes at the solid/water interface (Leus et al., 2017). Using the Langmuir adsorption
 335 model, we determined the maximum As adsorption capacities for both As species onto GR_{SO_4} (Table
 336 1). At alkaline pH, the maximum adsorption capacity of $As(III)$ was 2.2 times higher than the value at

337 neutral pH, while As(V) had 1.5 times higher maximum adsorption capacity at pH 7 compared to pH
 338 8-9.
 339



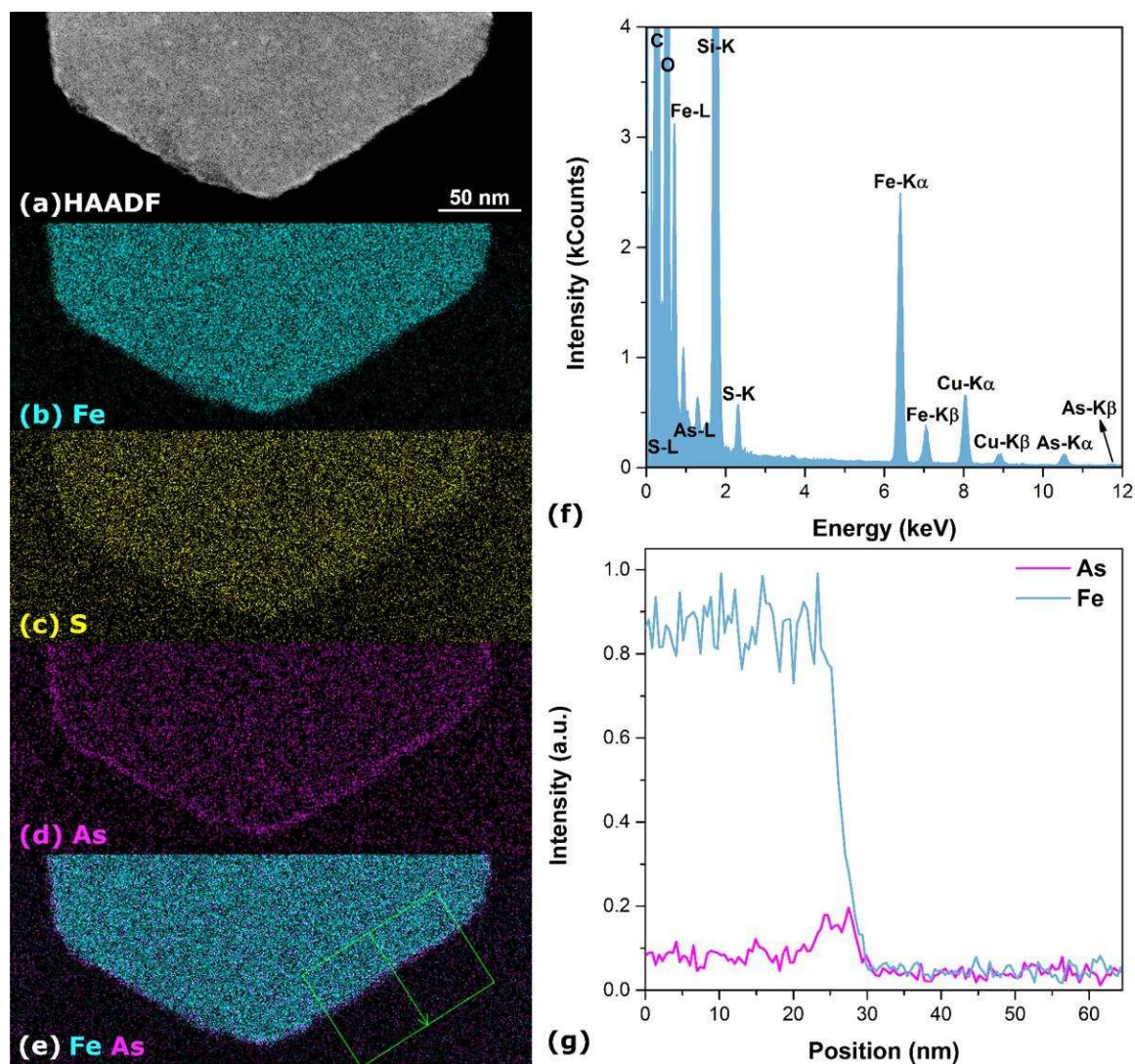
340 (c) 341 **Fig. 6.** Langmuir adsorption isotherms of As species on GR_{SO4}. (a-b) Adsorption of As(III) at pH 7
 342 and 8-9, respectively. (c-d) Adsorption of As(V) at pH 7 and 8-9, respectively. Error bars represent
 343 analytical uncertainty (< 5% relative) based on replicate measurements of QC solutions analyzed
 344 together with the samples (Table S1).

345

346 The spatial distribution of the adsorbed As(III) on the GR particles, at an initial concentration
 347 of 500 mg L⁻¹, was examined using HAADF-STEM imaging coupled with EDX mapping (Fig. 7).
 348 The EDX elemental map (Fig. 7d) and associated intensity profile (Fig. 7g) show higher
 349 concentrations of As can be found near the GR particle edges (*ca.* two times higher than the 001 GR
 350 surface). In addition, the HAADF-STEM image (Fig. 7a) alone shows increased intensity at the GR

351 particle edges which we interpret to be associated with increased As concentration. These results,
 352 combined with the adsorption isotherm results, strengthen previous findings that suggested that
 353 As(III) and As(V) form monodentate mononuclear (¹V) and bidentate binuclear (²C) inner-sphere
 354 complexes on the GR particle edges (Jönsson and Sherman, 2008; Wang et al., 2010). However, the
 355 maximum adsorption capacity for As(III) determined in the current study could also indicate that
 356 surface complexation may not be limited to the GR_{SO4} particle edges but, as mentioned before, may
 357 also result from the presence of multi-nuclear arsenite complexes (Ona-Nguema et al., 2009; Wang et
 358 al., 2010).

359



360
 361 **Fig. 7.** (a) HAADF-STEM overview of GR_{SO4} interacted with 500 mg L⁻¹ of As(III) and the
 362 corresponding (b) EDX elemental maps for (b) Fe (light blue), (c) S (yellow), (d) As (magenta) and

363 (e) combined Fe and As. (f) The EDX spectrum of (a). The Si signal comes from the use of headspace
364 crimp vials while C and Cu peaks come from the TEM grid. (g) The EDX signal intensity profile
365 shows the change in concentration of Fe and As along the integrated line drawn across the marked
366 area in green (e).

367

368 In addition to surface complexation, previous studies with selenate have shown that
369 tetrahedral oxyanions (e.g., SeO_4^{2-}) can also be removed by GR phases by interlayer intercalation
370 (Refait et al., 2000). In our study intercalation of As(III) and As(V) in the interlayer region of GR
371 would have resulted in changes in the basal spacing since the ionic radius of AsO_3^{3-} (2.11 Å) and
372 AsO_4^{3-} (2.48 Å) are different to that of SO_4^{2-} (2.30 Å) (Goh et al., 2008). However, XRD patterns of
373 GR_{SO_4} interacted with As(III) and As(V) at 10 mg L⁻¹ (Fig. 5a) and 500 mg L⁻¹ (Fig. S7) did not
374 exhibit shifts in the basal (001) reflections (~10.93 Å) to accommodate such intercalations. The
375 intercalation of As(III) and As(V) in our study, might have been inhibited because SO_4^{2-} cannot be
376 readily exchanged in layered double hydroxides (de Roy et al., 2001; Miyata, 1983).

377

378 3.6 Environmental significance of GR minerals in As-contaminated environments

379 Using the adsorption isotherm modelling data, we compared the calculated adsorption
380 capacities for As species on GR_{SO_4} and with literature data for all described iron (oxyhydr)oxides,
381 oxyhydroxysulfates and sulfides, which have also been evaluated for their efficiency as mineral
382 substrate for the treatment of As contaminated groundwater resources (Table 1).

383 Our data show clearly that GR_{SO_4} is among the most effective adsorbents among all the
384 phases listed in Table 1. This finding has important implications for the fate and mobility of As in
385 anoxic groundwaters where GR_{SO_4} exists. To the best of our knowledge, this is the first study to report
386 the adsorption isotherms of As(III) and As(V) for GR_{SO_4} , as well as the in-depth examination of
387 critical adsorption parameters for As removal. We have shown that at circum-neutral and slightly
388 alkaline pH conditions, GR_{SO_4} can efficiently adsorb large amounts of As(III) and As(V), making
389 GR_{SO_4} one of the best performing iron-bearing mineral phases in terms of As adsorption. For As(III)
390 at slightly alkaline pH, GR_{SO_4} is only outperformed by ferrihydrite (Table 1 entry 5) and

391 schwertmannite (Table 1 entry 6) (Davidson et al., 2008). Ferrihydrite and schwertmannite are poorly
 392 ordered, highly reactive and thermodynamically metastable iron-bearing mineral phases which can
 393 transform at ambient conditions to more thermodynamically stable crystalline iron (oxyhydr)oxides
 394 such as goethite and hematite, fast at alkaline conditions but slow at near-neutral pH values (Brinza et
 395 al., 2015; Burton et al., 2008; Davidson et al., 2008; Vu et al., 2013; Yee et al., 2006). Moreover,
 396 comparing our data with other Fe-bearing phases (Table 1) shows that among mixed-valent and
 397 redox-active iron (oxyhydr)oxides and sulphides, GR_{SO4} exhibits an unprecedented As(III) uptake and
 398 also remains stable for long time periods. Even compared to magnetite (Table 1 entry 4) and iron
 399 sulfides (e.g., troilite, pyrite; Table 1 entries 7-9) that are crystalline and highly stable in reduced
 400 environments, our GR_{SO4} showed higher adsorption capacities. This exceptional As adsorption
 401 capacity makes GR_{SO4} a novel and potentially highly environmentally-relevant mineral substrate for
 402 As sequestration in near-neutral pH and reduced to slightly oxidized groundwater systems.

403

404 **Table 1.** Comparison of As adsorption capacities of GR_{SO4} with common iron (oxyhydr)oxides,
 405 oxyhydroxy sulfates and sulfides.

Entry No.	Adsorbent	Particle size (nm)	Surface area (m ² g ⁻¹) ^a	Tested pH	Adsorption capacity (mg g ⁻¹)		Reference
					As(III)	As(V)	
1	Goethite	-	39	9	22.0	4.0	Lenoble et al. (2002)
2	Hematite	5	162	7	95.0	47.0	Tang et al. (2011)
3	Maghemite	7-12	169	-	67.0	95.4	Lin et al. (2012)
4	Magnetite	12	99	8	134.9	172.3	Yean et al. (2005)
5	Ferrihydrite	-	202	5	552.9	222.1	Raven et al. (1998)
6	Schwertmannite	-	280 ^b	9	280.4	166.5	Burton et al. (2009)
7	Mackinawite	2	350	7	9.7	32.2	Wolthers et al. (2005)
8	Troilite	-	3	7	17.3	-	Bostick and Fendorf (2003)
9	Pyrite	-	41	7	1.0	-	Bostick and Fendorf (2003)
10	GR _{CO3}	100-300	-	7.5	123.0	-	Su & Wilkin (2005)
11	GR _{SO4}	50-500	25 ^c	10.5	43.8	6.91	Su & Wilkin (2005)
				7	74.0	104.5	This work
				8-9	160.3	69.6	This work

406 ^aSpecific surface area determined by the Brunauer–Emmett–Teller (BET) model. ^b Estimated from Davidson et
407 al. (2008) ^c Measured nitrogen sorption isotherm can be found in Fig. S5.

408

409 Previous studies have shown that GR phases can oxidize As(III) to As(V) (Su and Puls, 2004;
410 Su and Wilkin, 2005). Although not investigated in this study, possible redox transformation can
411 heavily impact the toxicity and mobility of As in soils and groundwaters. As(III) oxidation by GR
412 mineral phases would be a favorable process as it would result in a less toxic and less mobile As(V)
413 species (Vaughan, 2006). On the other hand, reduction of As(V) to the far more toxic As(III) and the
414 potential re-release into groundwaters because of the lower affinity of As(III) for ferric iron
415 (oxyhydr)oxides would be far more damaging (Roberts et al., 2004). Further studies are needed to
416 confirm the potential of As(III) oxidation in the presence of GR and to determine the geochemical and
417 thermodynamic driving forces in this reaction.

418 As for redox-active mineral adsorbents, arsenic can still be released from GR_{SO4} since its
419 sequestration is highly dependent on pH conditions and redox environment. Sudden changes in pH or
420 Eh of the system may cause potential release of surface immobilized As species back into the
421 groundwater either by dissolution or redox-change driven transformation of GR phases (Cundy et al.,
422 2008). Iron mineral phases such as goethite and magnetite, which are common transformation end-
423 products of GR, are, however, far less reactive and effective mineral substrates for As sequestration
424 (Table 1), which can lead to remobilization of As in groundwaters.

425

426 **4. Conclusions**

427 In this work, we investigated the interfacial reactivity between GR_{SO4} and As species. An
428 extensive batch adsorption study was performed to examine the influence of various critical
429 environmental parameters such as initial concentration, pH, adsorbent loading, ionic strength and
430 presence of potentially interfering ions on As removal. We have successfully demonstrated that GR_{SO4}
431 is an effective and stable As(III) and As(V) mineral adsorbent compared to other iron (oxyhydr)oxide
432 phases. GR_{SO4} demonstrated remarkable maximum adsorption capacities for As(III) and As(V) of up
433 to 160 and 105 mg g⁻¹, respectively. This exceptional As adsorption reactivity makes GR a potentially

434 novel and environmentally-relevant mineral substrate for the sequestration of As in reduced
435 groundwater systems. The removal of As is also highly pH dependent – high As(III) removal was
436 obtained at higher pH while As(V) removal was found to be more favourable at circum-neutral
437 conditions. GR_{SO4} exhibited fast As uptake rates at alkaline conditions. Common groundwater species
438 such as Mg²⁺ and PO₄³⁻ were found to affect the efficiency of As adsorption onto GR_{SO4}. Overall, our
439 results clearly highlight importance of redox-active GR mineral phases in removing As species from
440 aqueous solutions and their potential crucial role in the remediation of contaminated groundwaters.

441

442 **Acknowledgement**

443 This project has received funding from the European Union's Horizon 2020 Marie
444 Sklodowska-Curie Innovative Training Network Grant No. 675219 for JPHP and LGB and the
445 German Helmholtz Recruiting Initiative funding to LGB and HMF. ICP-OES analyses were carried
446 out at the Helmholtz Laboratory for the Geochemistry of the Earth Surface (HELGES), GFZ Potsdam.
447 We thank Rogier Besselink from the Interface Geochemistry Section at GFZ for the help with the
448 BET analyses; Andrea Vieth-Hillebrand from the Organic Geochemistry Section at GFZ for the help
449 with ion chromatography analysis; and Andy Brown from the Leeds Electron Microscopy and
450 Spectroscopy Centre (LEMAS), University of Leeds, for the help with electron diffraction and EDX
451 mapping, and for providing reference EEL spectra for hedenbergite and hematite samples. We also
452 acknowledge the help of Jörg Radnik from the German Federal Institute for Materials Research and
453 Testing (BAM) with the XPS analyses and of Peter Adler from the Max Planck Institute for Chemical
454 Physics of Solids for the Mössbauer analysis. XRD analyses were done with the assistance of Marco
455 Mangayayam and Dominique J. Tobler from NanoGeoScience, University of Copenhagen. The
456 authors would also like to thank Robin Wojcik of the Interface Geochemistry Section at GFZ for his
457 help in the graphical abstract.

458

459 **Appendix A. Supplementary data**

460 Details on mineral characterization and data (XRD, TEM, SAED, EDX, EELS, N₂ sorption,
461 XPS, Mössbauer spectroscopy, ICP-OES, ion chromatography), batch adsorption experimental

462 methods and data and aqueous concentration analysis of long-term batch experiments can be found in
463 the Supporting Information. Supplementary data associated with this article can be found in the online
464 version.

465

466 **References**

- 467 Ahmed IAM, Benning LG, Kakonyi G, Sumoondur AD, Terrill NJ, Shaw S. Formation of green rust
468 sulfate: A combined in situ time-resolved X-ray scattering and electrochemical study. *Langmuir*
469 2010; 26: 6593-6603.
- 470 Ahmed IAM, Shaw S, Benning LG. Formation of hydroxysulphate and hydroxycarbonate green rusts
471 in the presence of zinc using time-resolved in situ small and wide angle X-ray scattering.
472 *Mineralogical Magazine* 2008; 72: 159-162.
- 473 Asere TG, De Clercq J, Verbeken K, Tessema DA, Fufa F, Stevens CV, et al. Uptake of arsenate by
474 aluminum (hydr)oxide coated red scoria and pumice. *Applied Geochemistry* 2017; 78: 83-95.
- 475 Bocher F, Géhin A, Ruby C, Ghanbaja J, Abdelmoula M, Génin J-MR. Coprecipitation of Fe(II-III)
476 hydroxycarbonate green rust stabilised by phosphate adsorption. *Solid State Sciences* 2004; 6:
477 117-124.
- 478 Bostick BC, Fendorf S. Arsenite sorption on troilite (FeS) and pyrite (FeS₂). *Geochimica et*
479 *Cosmochimica Acta* 2003; 67: 909-921.
- 480 Brinza L, Vu HP, Shaw S, Mosselmans JFW, Benning LG. Effect of Mo and V on the hydrothermal
481 crystallization of hematite from ferrihydrite: An in situ energy dispersive X-ray diffraction and
482 X-ray absorption spectroscopy study. *Crystal Growth & Design* 2015; 15: 4768-4780.
- 483 Brown AP, Hillier S, Brydson RMD. Quantification of Fe-oxidation state in mixed valence minerals:
484 a geochemical application of EELS revisited. *Journal of Physics: Conference Series* 2017; 902:
485 012016.
- 486 Burton ED, Bush RT, Johnston SG, Watling KM, Hocking RK, Sullivan LA, et al. Sorption of
487 arsenic(V) and arsenic(III) to schwertmannite. *Environmental Science & Technology* 2009; 43:
488 9202-9207.
- 489 Burton ED, Bush RT, Sullivan LA, Mitchell DRG. Schwertmannite transformation to goethite via the
490 Fe(II) pathway: Reaction rates and implications for iron-sulfide formation. *Geochimica et*
491 *Cosmochimica Acta* 2008; 72: 4551-4564.
- 492 Christiansen BC, Balic-Zunic T, Petit PO, Frandsen C, Mørup S, Geckeis H, et al. Composition and
493 structure of an iron-bearing, layered double hydroxide (LDH) – Green rust sodium sulphate.
494 *Geochimica et Cosmochimica Acta* 2009; 73: 3579-3592.
- 495 Christiansen BC, Geckeis H, Marquardt CM, Bauer A, Römer J, Wiss T, et al. Neptunyl (Np)
496 interaction with green rust. *Geochimica et Cosmochimica Acta* 2011; 75: 1216-1226.
- 497 Cundy AB, Hopkinson L, Whitby RLD. Use of iron-based technologies in contaminated land and
498 groundwater remediation: A review. *Science of The Total Environment* 2008; 400: 42-51.
- 499 Davidson LE, Shaw S, Benning LG. The kinetics and mechanisms of schwertmannite transformation
500 to goethite and hematite under alkaline conditions. *American Mineralogist* 2008; 93: 1326.
- 501 de Roy A, Forano C, Besse JP. Layered Double Hydroxides: Synthesis and Post-Synthesis
502 Modification. In: Rives V, editor. *Layered Double Hydroxides: Present and Future*. Nova
503 Science Publishers, New York, 2001, pp. 1-39.
- 504 Ferguson JF, Gavis J. A review of the arsenic cycle in natural waters. *Water Research* 1972; 6: 1259-
505 1274.
- 506 Folens K, Leus K, Nicomel NR, Meledina M, Turner S, Van Tendeloo G, et al. Fe₃O₄@MIL-101 - A
507 selective and regenerable adsorbent for the removal of As species from water. *European Journal*
508 *of Inorganic Chemistry* 2016: 4395-4401.
- 509 Géhin A, Ruby C, Abdelmoula M, Benali O, Ghanbaja J, Refait P, et al. Synthesis of Fe(II-III)
510 hydroxysulphate green rust by coprecipitation. *Solid State Sciences* 2002; 4: 61-66.

511 Génin J-MR, Ruby C. Anion and cation distributions in Fe(II–III) hydroxysalt green rusts from XRD
512 and Mössbauer analysis (carbonate, chloride, sulphate, ...); the “fougerite” mineral. *Solid State*
513 *Sciences* 2004; 6: 705-718.

514 Goh K-H, Lim T-T, Dong Z. Application of layered double hydroxides for removal of oxyanions: A
515 review. *Water Research* 2008; 42: 1343-1368.

516 Guilbaud R, White ML, Poulton SW. Surface charge and growth of sulphate and carbonate green rust
517 in aqueous media. *Geochimica et Cosmochimica Acta* 2013; 108: 141-153.

518 Guo X, Chen F. Removal of Arsenic by Bead Cellulose Loaded with Iron Oxyhydroxide from
519 Groundwater. *Environmental Science & Technology* 2005; 39: 6808-6818.

520 Gupta A, Chauhan VS, Sankararamakrishnan N. Preparation and evaluation of iron–chitosan
521 composites for removal of As(III) and As(V) from arsenic contaminated real life groundwater.
522 *Water Research* 2009; 43: 3862-3870.

523 Ho Y-S. Review of second-order models for adsorption systems. *Journal of Hazardous Materials*
524 2006; 136: 681-689.

525 Hongshao Z, Stanforth R. Competitive adsorption of phosphate and arsenate on goethite.
526 *Environmental Science & Technology* 2001; 35: 4753-4757.

527 Hughes MF. Arsenic toxicity and potential mechanisms of action. *Toxicology Letters* 2002; 133: 1-
528 16.

529 Inskip WP, McDermott TR, Fendorf S. Arsenic (V)/(III) recycling in soils and natural waters:
530 Chemical and microbiological processes. In: Frankenberger WT, editor. *Environmental*
531 *Chemistry of Arsenic*. Marcel Dekker, New York, 2002, pp. 183-215.

532 Jain A, Raven KP, Loeppert RH. Arsenite and Arsenate Adsorption on Ferrihydrite: Surface Charge
533 Reduction and Net OH- Release Stoichiometry. *Environmental Science & Technology* 1999;
534 33: 1179-1184.

535 Jönsson J, Sherman DM. Sorption of As(III) and As(V) to siderite, green rust (fougerite) and
536 magnetite: Implications for arsenic release in anoxic groundwaters. *Chemical Geology* 2008;
537 255: 173-181.

538 Lenoble V, Bouras O, Deluchat V, Serpaud B, Bollinger J-C. Arsenic adsorption onto pillared clays
539 and iron oxides. *Journal of Colloid and Interface Science* 2002; 255: 52-58.

540 Leus K, Folens K, Nicomel NR, Perez JPH, Filippousi M, Meledina M, et al. Removal of arsenic and
541 mercury species from water by covalent triazine framework encapsulated γ -Fe₂O₃
542 nanoparticles. *Journal of Hazardous Materials* 2018; 353: 312-319.

543 Leus K, Perez JPH, Folens K, Meledina M, Van Tendeloo G, Du Laing G, et al. UiO-66-(SH)₂ as
544 stable, selective and regenerable adsorbent for the removal of mercury from water under
545 environmentally-relevant conditions. *Faraday Discussions* 2017; 201: 145-161.

546 Lightstone FC, Schwegler E, Hood RQ, Gygi F, Galli G. A first principles molecular dynamics
547 simulation of the hydrated magnesium ion. *Chemical Physics Letters* 2001; 343: 549-555.

548 Limousin G, Gaudet JP, Charlet L, Szenknect S, Barthès V, Krimissa M. Sorption isotherms: A
549 review on physical bases, modeling and measurement. *Applied Geochemistry* 2007; 22: 249-
550 275.

551 Lin S, Lu D, Liu Z. Removal of arsenic contaminants with magnetic γ -Fe₂O₃ nanoparticles. *Chemical*
552 *Engineering Journal* 2012; 211–212: 46-52.

553 Malis T, Cheng SC, Egerton RF. EELS log-ratio technique for specimen-thickness measurement in
554 the TEM. *Journal of Electron Microscopy Technique* 1988; 8: 193-200.

555 Masscheleyn PH, Delaune RD, Patrick WH. Arsenic and selenium chemistry as affected by sediment
556 redox potential and pH. *Journal of Environmental Quality* 1991; 20: 522-527.

557 Mitsunobu S, Takahashi Y, Sakai Y, Inumaru K. Interaction of synthetic sulfate green rust with
558 antimony(V). *Environmental Science & Technology* 2009; 43: 318-323.

559 Miyata S. Anion-exchange properties of hydrotalcite-like compounds. *Clays Clay Miner* 1983; 31:
560 305-311.

561 Mullet M, Guillemin Y, Ruby C. Oxidation and deprotonation of synthetic Fe^{II}-Fe^{III}
562 (oxy)hydroxycarbonate Green Rust: An X-ray photoelectron study. *Journal of Solid State*
563 *Chemistry* 2008; 181: 81-89.

564 Nedel S, Dideriksen K, Christiansen BC, Bovet N, Stipp SLS. Uptake and release of cerium during
565 Fe-oxide formation and transformation in Fe(II) solutions. *Environmental Science &*
566 *Technology* 2010; 44: 4493-4498.

567 Nickson RT, McArthur JM, Ravenscroft P, Burgess WG, Ahmed KM. Mechanism of arsenic release
568 to groundwater, Bangladesh and West Bengal. *Applied Geochemistry* 2000; 15: 403-413.

569 O'Loughlin EJ, Kelly SD, Cook RE, Csencsits R, Kemner KM. Reduction of uranium(VI) by mixed
570 iron(II)/iron(III) hydroxide (green rust): Formation of UO₂ nanoparticles. *Environmental*
571 *Science & Technology* 2003; 37: 721-727.

572 Ona-Nguema G, Morin G, Wang Y, Menguy N, Juillot F, Olivi L, et al. Arsenite sequestration at the
573 surface of nano-Fe(OH)₂, ferrous-carbonate hydroxide, and green-rust after bioreduction of
574 arsenic-sorbed lepidocrocite by *Shewanella putrefaciens*. *Geochimica et Cosmochimica Acta*
575 2009; 73: 1359-1381.

576 Randall SR, Sherman DM, Ragnarsdottir KV. Sorption of As(V) on green rust
577 (Fe₄(II)Fe₂(III)(OH)₁₂SO₄ · 3H₂O) and lepidocrocite (γ-FeOOH): Surface complexes from
578 EXAFS spectroscopy. *Geochimica et Cosmochimica Acta* 2001; 65: 1015-1023.

579 Raven KP, Jain A, Loeppert RH. Arsenite and arsenate adsorption on ferrihydrite: Kinetics,
580 equilibrium, and adsorption envelopes. *Environmental Science & Technology* 1998; 32: 344-
581 349.

582 Refait P, Bauer P, Olowe AA, Genin JMR. The substitution of Fe²⁺ ions by Ni²⁺ ions in the green rust
583 2 compound studied by Mössbauer effect. *Hyperfine Interactions* 1990; 57: 2061-2066.

584 Refait P, Simon L, Génin J-MR. Reduction of SeO₄²⁻ anions and anoxic formation of iron(II)-iron(III)
585 hydroxy-selenate green rust. *Environmental Science & Technology* 2000; 34: 819-825.

586 Roberts LC, Hug SJ, Ruettimann T, Billah MM, Khan AW, Rahman MT. Arsenic removal with
587 iron(II) and iron(III) in waters with high silicate and phosphate concentrations. *Environmental*
588 *Science & Technology* 2004; 38: 307-315.

589 Schuessler JA, Kämpf H, Koch U, Alawi M. Earthquake impact on iron isotope signatures recorded in
590 mineral spring water. *Journal of Geophysical Research: Solid Earth* 2016; 121: 8548-8568.

591 Sharma VK, Sohn M. Aquatic arsenic: Toxicity, speciation, transformations, and remediation.
592 *Environment International* 2009; 35: 743-759.

593 Shipley HJ, Yean S, Kan AT, Tomson MB. Adsorption of arsenic to magnetite nanoparticles: Effect
594 of particle concentration, pH, ionic strength, and temperature. *Environmental Toxicology and*
595 *Chemistry* 2009; 28: 509-515.

596 Simon L, François M, Refait P, Renaudin G, Lelaurain M, Génin J-MR. Structure of the Fe(II-III)
597 layered double hydroxysulphate green rust two from Rietveld analysis. *Solid State Sciences*
598 2003; 5: 327-334.

599 Skovbjerg LL, Stipp SLS, Utsunomiya S, Ewing RC. The mechanisms of reduction of hexavalent
600 chromium by green rust sodium sulphate: Formation of Cr-goethite. *Geochimica et*
601 *Cosmochimica Acta* 2006; 70: 3582-3592.

602 Smedley PL, Kinniburgh DG. A review of the source, behaviour and distribution of arsenic in natural
603 waters. *Applied Geochemistry* 2002; 17: 517-568.

604 Su C, Puls RW. Significance of iron(II,III) hydroxycarbonate green rust in arsenic remediation using
605 zerovalent iron in laboratory column tests. *Environmental Science & Technology* 2004; 38:
606 5224-5231.

607 Su C, Wilkin RT. Arsenate and arsenite sorption on and arsenite oxidation by iron(II, III)
608 hydroxycarbonate green rust. *Advances in Arsenic Research*. 915. American Chemical Society,
609 2005, pp. 25-40.

610 Tang W, Li Q, Gao S, Shang JK. Arsenic (III,V) removal from aqueous solution by ultrafine α-Fe₂O₃
611 nanoparticles synthesized from solvent thermal method. *Journal of Hazardous Materials* 2011;
612 192: 131-138.

613 Usman M, Byrne JM, Chaudhary A, Orsetti S, Hanna K, Ruby C, et al. Magnetite and green rust:
614 Synthesis, properties, and environmental applications of mixed-valent iron minerals. *Chemical*
615 *Reviews* 2018; 118: 3251-3304.

616 Vaughan DJ. Arsenic. *Elements* 2006; 2: 71-75.

- 617 Vu HP, Shaw S, Brinza L, Benning LG. Partitioning of Pb(II) during goethite and hematite
618 crystallization: Implications for Pb transport in natural systems. *Applied Geochemistry* 2013;
619 39: 119-128.
- 620 Wang Y, Morin G, Ona-Nguema G, Brown GE. Arsenic(III) and arsenic(V) speciation during
621 transformation of lepidocrocite to magnetite. *Environmental Science & Technology* 2014; 48:
622 14282-14290.
- 623 Wang Y, Morin G, Ona-Nguema G, Juillot F, Guyot F, Calas G, et al. Evidence for different surface
624 speciation of arsenite and arsenate on green rust: An EXAFS and XANES Study.
625 *Environmental Science & Technology* 2010; 44: 109-115.
- 626 Williams M, Fordyce F, Pajitrapapon A, Charoensaisri P. Arsenic contamination in surface
627 drainage and groundwater in part of the southeast Asian tin belt, Nakhon Si Thammarat
628 Province, southern Thailand. *Environmental Geology* 1996; 27: 16-33.
- 629 Wolthers M, Charlet L, van Der Weijden CH, van der Linde PR, Rickard D. Arsenic mobility in the
630 ambient sulfidic environment: Sorption of arsenic(V) and arsenic(III) onto disordered
631 mackinawite. *Geochimica et Cosmochimica Acta* 2005; 69: 3483-3492.
- 632 World Health Organization. Guidelines for drinking-water quality: Fourth edition incorporating the
633 first addendum. Geneva, 2017.
- 634 Yean S, Cong L, Yavuz CT, Mayo JT, Yu WW, Kan AT, et al. Effect of magnetite particle size on
635 adsorption and desorption of arsenite and arsenate. *Journal of Materials Research* 2005; 20:
636 3255-3264.
- 637 Yee N, Shaw S, Benning LG, Nguyen TH. The rate of ferrihydrite transformation to goethite via the
638 Fe(II) pathway. *American Mineralogist* 2006; 91: 92-96.
- 639 Zahid A, Hassan MQ, Balke KD, Flegr M, Clark DW. Groundwater chemistry and occurrence of
640 arsenic in the Meghna floodplain aquifer, southeastern Bangladesh. *Environmental Geology*
641 2008; 54: 1247-1260.
- 642